Describing the Shape of Raindrop Size Distributions Using Uncorrelated Raindrop Mass Spectrum Parameters

CHRISTOPHER R. WILLIAMS,[a] V. N. BRINGI,[b] LAWRENCE D. CAREY,[c] V. CHANDRASEKAR,[b] PATRICK N. GATLIN,[d] ZIAD S. HADDAD,[e] ROBERT MENEGHINI,[f] S. JOSEPH MUNCHAK,[g] STEPHEN W. NESBITT,[h] WALTER A. PETERSEN,[i] SIMONE TANELLI,[e] ALI TOKAY,[j] ANNA WILSON,[k] AND DAVID B. WOLFF[i]

[a] *Cooperative Institute for Research in Environmental Sciences, University of Colorado Boulder, and NOAA/ESRL Physical Sciences Division, Boulder, Colorado*
[b] *Colorado State University, Fort Collins, Colorado*
[c] *University of Alabama in Huntsville, Huntsville, Alabama*
[d] *NASA Marshall Space Flight Center, Huntsville, Alabama*
[e] *Jet Propulsion Laboratory, California Institute of Technology, Pasadena, California*
[f] *NASA Goddard Space Flight Center, Greenbelt, Maryland*
[g] *University of Maryland, College Park, College Park, Maryland*
[h] *University of Illinois at Urbana–Champaign, Urbana, Illinois*
[i] *NASA Goddard Space Flight Center Wallops Flight Facility, Wallops Island, Virginia*
[j] *University of Maryland, Baltimore County, Greenbelt, Maryland*
[k] *Duke University, Durham, North Carolina*

(Manuscript received 28 February 2013, in final form 15 January 2014)

ABSTRACT

Rainfall retrieval algorithms often assume a gamma-shaped raindrop size distribution (DSD) with three mathematical parameters N_w, D_m, and μ. If only two independent measurements are available, as with the dual-frequency precipitation radar on the Global Precipitation Measurement (GPM) mission core satellite, then retrieval algorithms are underconstrained and require assumptions about DSD parameters. To reduce the number of free parameters, algorithms can assume that μ is either a constant or a function of D_m. Previous studies have suggested μ–Λ constraints [where $\Lambda = (4 + \mu)/D_m$], but controversies exist over whether μ–Λ constraints result from physical processes or mathematical artifacts due to high correlations between gamma DSD parameters. This study avoids mathematical artifacts by developing joint probability distribution functions (joint PDFs) of statistically independent DSD attributes derived from the raindrop mass spectrum. These joint PDFs are then mapped into gamma-shaped DSD parameter joint PDFs that can be used in probabilistic rainfall retrieval algorithms as proposed for the GPM satellite program. Surface disdrometer data show a high correlation coefficient between the mass spectrum mean diameter D_m and mass spectrum standard deviation σ_m. To remove correlations between DSD attributes, a normalized mass spectrum standard deviation σ'_m is constructed to be statistically independent of D_m, with $\overline{\sigma'_m}$ representing the most likely value and std(σ'_m) representing its dispersion. Joint PDFs of D_m and μ are created from D_m and σ'_m. A simple algorithm shows that rain-rate estimates had smaller biases when assuming the DSD breadth of $\overline{\sigma'_m}$ than when assuming a constant μ.

1. Introduction

Building on the successful Tropical Rainfall Measuring Mission (TRMM), the Global Precipitation Measurement (GPM) mission aims to use multiple satellites to estimate surface rainfall with a 3-h resolution between 65°S and 65°N (Hou et al. 2008). The core GPM satellite will observe precipitation with a cross-track scanning dual-frequency precipitation radar (DPR) and a conically scanning multiple-frequency radiometer. The constellation of GPM satellites will observe precipitation with passive microwave sensors (Huffman et al. 2007).

Algorithms will estimate surface rainfall by using different combinations of GPM observations. "Radar only" algorithms will use DPR observations (e.g., Grecu et al.

Corresponding author address: Christopher R. Williams, Cooperative Institute for Research in Environmental Sciences, University of Colorado Boulder, 216 UCB, Boulder, CO 80309-0216.
E-mail: christopher.williams@colorado.edu

DOI: 10.1175/JAMC-D-13-076.1

© 2014 American Meteorological Society

2011), "radiometer only" algorithms will use passive microwave observations (e.g., Kummerow et al. 2011), and "combined" algorithms will use both radar and radiometer observations (e.g., Munchak and Kummerow 2011). Algorithms will use probabilistic frameworks that seek to reproduce the observed reflectivities and/or radiances with physically realistic raindrop size distributions (DSDs) following either Bayesian theory (Haddad et al. 2006) or optimal estimation theory (Munchak and Kummerow 2011).

To estimate surface rainfall, retrieval algorithms often assume that the DSD follows a gamma-shaped distribution with three parameters (e.g., Rose and Chandrasekar 2006; Iguchi et al. 2009; Kozu et al. 2009; Grecu et al. 2011; Munchak and Kummerow 2011; Seto and Iguchi 2011; Seto et al. 2013). In the ideal case, three measurements are needed to constrain three unknowns. When only two measurements are available, as in DPR observations (e.g., absolute reflectivity at two radar operating wavelengths), assumptions are needed to constrain the third DSD parameter.

A simple, yet problematic formulation of a gamma-shaped distribution was introduced by Ulbrich (1983):

$$N(D) = N_0 D^{\mu} \exp(-\Lambda D), \tag{1}$$

where $N(D)$ is the raindrop concentration representing the number of raindrops per diameter interval per unit volume ($\mathrm{mm}^{-1}\,\mathrm{m}^{-3}$); D is the raindrop diameter (mm); and N_0 ($\mathrm{mm}^{-1-\mu}\,\mathrm{m}^{-3}$), Λ (mm^{-1}), and μ (unitless) are the "scale," "slope," and "shape" parameters, respectively. These three parameters are *mathematical parameters* because they do not represent physical quantities unless $\mu = 0$, which is the inverse exponential case. Several studies have shown that these three mathematical parameters are not statistically independent but are correlated, with high Pearson correlation coefficients (Ulbrich 1983; Ulbrich and Atlas 1985; Chandrasekar and Bringi 1987; Moisseev and Chandrasekar 2007; Illingworth and Blackman 2002). By exploiting the correlations between μ and Λ, Zhang et al. (2001, 2003) developed a μ–Λ relationship:

$$\Lambda = 0.0365\mu^2 + 0.735\mu + 1.935, \tag{2}$$

so that the three-parameter DSD in Eq. (1) is described as a "constrained DSD" with two free parameters and a μ–Λ constraint. Using a μ–Λ constraint improved rainfall estimates from polarimetric radar because two radar measurements, reflectivity factor Z and differential reflectivity Z_{dr}, are used to solve for the two free DSD parameters in the constrained DSD (Cao and Zhang 2009). Over the past few years, studies found that μ–Λ relationships vary with rain microphysics (Atlas and Ulbrich 2006) and with radar reflectivity (Munchak and Tokay 2008). Studies have also shown that radar rainfall estimates improve after adjusting the μ–Λ relationship to ground observations (Cao et al. 2008). In aggregate, these prior studies suggest that a μ–Λ constraint improves rain-rate estimates, but a single μ–Λ relationship does not describe the storm-to-storm or within-storm rain microphysics variability that modifies the DSD shape.

There is concern that μ–Λ relationships similar to Eq. (2) result from mathematical artifacts due to correlations between the three mathematical parameters in Eq. (1) (Chandrasekar and Bringi 1987; Moisseev and Chandrasekar 2007). Another concern is that surface disdrometer observations used in developing μ–Λ relationships may underestimate the number of small raindrops in rain because of wind blowing small raindrops around the instrument inlet or low instrument sensitivity to detecting small raindrops (Moisseev and Chandrasekar 2007). The limited detection of small raindrops causes truncated raindrop spectra that lead to narrower spectra and biased μ–Λ relationships. Even if μ–Λ relationships contain mathematical artifacts, Zhang et al. (2003) have argued that μ–Λ relationships contain physical meaning and lead to improved rain-rate estimates [as later documented by Cao and Zhang (2009)].

Even without concerns over mathematical artifacts, single-value μ–Λ relationships as in Eq. (2) cannot be used in probabilistic rainfall retrieval algorithms because they only provide the expected (or initial) value of a DSD constraint. Probabilistic algorithms need the expected value *plus* a range of acceptable values to converge to a final solution (Haddad et al. 2006; Munchak and Kummerow 2011). The National Aeronautics and Space Administration (NASA) Precipitation Measurement Missions (PMM) DSD Working Group[1] is investigating whether the DSD constraints, or assumptions, used in rainfall retrieval algorithms are observed in field campaign raindrop spectra and whether new constraints can be constructed that fit probabilistic algorithm logic. This study focuses on developing probabilistic DSD constraints through analysis of disdrometer observations. Developing probabilistic algorithms will be described elsewhere (e.g., Munchak and Kummerow 2011).

The DSD Working Group is investigating new DSD constraints by rephrasing the problem in two key ways. First, to avoid mathematical artifacts, relationships between directly measurable *physical attributes* of the DSD are investigated, and relationships between fitted

[1] The DSD Working Group is composed of NASA PMM Science Team members and includes GPM algorithm developers and observational scientists.

mathematical parameters of a gamma function are not investigated. Since gamma parameters are not statistically independent, mathematical artifacts will appear in relationships once a DSD is assumed to follow a gamma mathematical model. Second, the relationships between physical DSD attributes are expressed in terms of joint probability distribution functions (joint PDFs) and not only as a best-fit line. The problem is now rephrased as, Given an algorithm estimate of one DSD physical attribute, what is the expected value and range of another DSD physical attribute? After determining joint PDFs of statistically independent DSD physical attributes, joint PDFs of gamma model parameters are constructed so that physically based constraints can be used in probabilistic rainfall retrieval algorithms that are formulated using gamma-shaped DSDs.

This study has the following structure: After defining a normalized gamma DSD, a simple dual-frequency radar rain-rate algorithm is described to highlight how a constraint, or assumption, is needed in the algorithm to solve the three-parameter DSD when only two measurements are available. *Without an assumption of a gamma-shaped DSD a priori*, section 3 uses the raindrop mass spectrum mean diameter D_m and standard deviation σ_m to describe the DSD shape. Surface disdrometer observations are introduced in section 4, and in section 5 a power-law relationship between estimated D_m and σ_m is removed to construct a new mass spectrum standard deviation estimate σ'_m that is statistically independent of D_m. The DSD shape can now be defined by two uncorrelated physical attributes: D_m and σ'_m. From the definition of gamma-shaped DSDs, a transformation, or mapping, is generated between (D_m, σ'_m) and gamma parameters (D_m, μ). Section 6 uses the simple rain-rate algorithm from section 2 to show that the rain rates estimated with the most likely, or expected, value of the new power-law D_m–μ constraint have smaller biases than when a constant μ value is assumed. Section 7 presents some conclusions and proposes future work.

2. Gamma-shaped DSD and a simple DPR algorithm

This section describes the assumptions a simple rainfall retrieval algorithm needs to make when it has two radar input measurements and models the DSD with three parameters. This simple algorithm follows the GPM DPR rainfall algorithm general logic (Seto et al. 2013), but only at a single altitude and without attenuation correction. Because the gamma function parameters N_0, Λ, and μ used in Eq. (1) are highly correlated, using normalized gamma function parameters (defined below as N_w, D_m, and μ) should help to reduce the mathematical artifacts between DSD parameters (Testud et al. 2001; Illingworth and Blackman 2002; Bringi et al. 2003). In constructing DPR algorithms, it is convenient to rewrite the normalized gamma DSD model as a scaled quasi PDF with the form (Chandrasekar et al. 2005; Seto et al. 2013)

$$N(D; N_w, D_m, \mu) = N_w f(D; D_m, \mu), \tag{3}$$

where

$$N_w = \frac{4^4}{\pi \rho_w}\left(\frac{q}{D_m^4}\right), \tag{4}$$

$$f(D; D_m, \mu) = \frac{6}{4^4}\frac{(4+\mu)^{\mu+4}}{\Gamma(\mu+4)}\left(\frac{D}{D_m}\right)^{\mu}\exp\left[-(4+\mu)\left(\frac{D}{D_m}\right)\right], \tag{5}$$

D is the raindrop equivalent spherical diameter (mm), ρ_w is the density of water (1 g cm^{-3}), q is the liquid water content (g m^{-3}) given by

$$q = \frac{\pi}{6\times 10^3}\rho_w \sum_{D_{\min}}^{D_{\max}} N(D) D^3\, dD, \tag{6}$$

$\Gamma()$ is the gamma function, and D_m (mm) is defined as

$$D_m = \frac{\sum_{D_{\min}}^{D_{\max}} N(D) D^4\, dD}{\sum_{D_{\min}}^{D_{\max}} N(D) D^3\, dD}. \tag{7}$$

The summations extend from the minimum to the maximum diameters (from $D_{\min}$ to $D_{\max}$) with raindrop diameter interval dD. The variable N_w acts to scale the DSD concentration, and D_m and μ determine the DSD shape. The function $f(D; D_m, \mu)$ is called a quasi PDF because the magnitude of the integral over all D depends on D_m and μ whereas the integral of a true PDF is unity.

Following Seto et al. (2013), the scaled quasi PDF allows the effective radar reflectivity factor [denoted by Z_e (mm^6 m^{-3})] to be estimated using

$$Z_e = N_w F(D_m, \mu), \tag{8}$$

where

$$F(D_m, \mu) = \frac{\lambda^4}{\pi^5}\left|\frac{n_w^2+2}{n_w^2-1}\right|^2 \sum_{D_{\min}}^{D_{\max}} \sigma_{b,\lambda}(D) f(D; D_m, \mu)\, dD, \tag{9}$$

$\sigma_{b,\lambda}$ is the backscattering cross section (mm^2) at radar wavelength λ (mm), and n_w is the refractivity index of

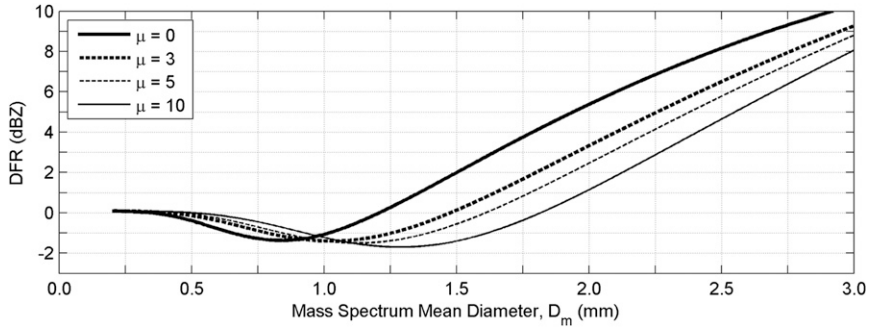

FIG. 1. Dual-frequency ratio (DFR) (dBZ) vs D_m calculated at 13.6- (Ku band) and 35.5-GHz (Ka band) radar frequencies using DFR = $10\log_{10}(Z_e^{\mathrm{Ku}}) - 10\log_{10}(Z_e^{\mathrm{Ka}})$. DFR is estimated for μ values of 0, 3, 5, and 10.

water in liquid phase. The DPR on the GPM satellite will observe the same precipitation volume at 13.6 and 35.5 GHz (denoted as Ku and Ka bands, respectively) in the inner swath of the Ku-band radar. The quasi-PDF notation allows the dual-frequency ratio of reflectivity [denoted as DFR (dBZ)] at the DPR frequencies to be independent of N_w and a function of only D_m and μ:

$$\mathrm{DFR}(D_m,\mu) = 10\log_{10}\left(\frac{Z_e^{\mathrm{Ku}}}{Z_e^{\mathrm{Ka}}}\right) = 10\log_{10}\left[\frac{F^{\mathrm{Ku}}(D_m,\mu)}{F^{\mathrm{Ka}}(D_m,\mu)}\right], \tag{10a}$$

which can be written as

$$\mathrm{DFR}(D_m,\mu) = 10\log_{10}[F^{\mathrm{Ku}}(D_m,\mu)] - 10\log_{10}[F^{\mathrm{Ka}}(D_m,\mu)], \tag{10b}$$

where the superscripts Ka and Ku indicate the value for the Ka- and Ku-band frequencies estimated using wavelength-dependent parameters in Eq. (9). Calculating DFR(D_m, μ) with known values of D_m and μ is straightforward and is shown in Fig. 1 with μ equal to 0, 3, 5, and 10, but a DPR retrieval algorithm using radar-measured reflectivities at Ka- and Ku-band frequencies must estimate D_m and μ from estimates of attenuation corrected reflectivities Z_e^{Ku} and Z_e^{Ka} [attenuation correction involves many calculations and algorithm-dependent assumptions that are not discussed here; see Seto et al. (2013) for details]. Without any prior information, retrieval algorithms assume a μ value and then D_m is estimated from a DFR(D_m, μ) lookup table constructed using Eq. (10) (note that in some cases multiple values of D_m may represent valid solutions).

The scale parameter N_w is then estimated by rearranging Eq. (8) and using either the estimated Z_e^{Ku} or Z_e^{Ka}. For Ku-band observations, N_w is estimated using

$$N_w = \frac{Z_e^{\mathrm{Ku}}}{F^{\mathrm{Ku}}(D_m,\mu)}. \tag{11}$$

The retrieval algorithm can now estimate rain rate R using

$$R = \frac{6\pi}{10^3}\sum_{D_{\min}}^{D_{\max}} N_{\mathrm{w}} f(D;D_m,\mu)D^3 v(D)\,dD, \tag{12}$$

where $v(D)$ (m s^{-1}) is the fall speed of raindrops with diameter D (mm). Section 6 will use this simple retrieval algorithm to show improved rain-rate estimates by assuming μ is a function of D_m rather than assuming μ is a constant.

3. Attributes of the raindrop mass spectrum

In the previous section, the DSD was modeled with a modified gamma function using parameters N_w, D_m, and μ. In this section, the DSD is not assumed to have any a priori shape but is expressed as a raindrop number concentration $N(D)$ observed by a surface disdrometer with discrete diameter size bins. By expressing the DSDs as raindrop mass spectra, the shape of the discrete distribution can be described by two attributes: the mass-weighted mean diameter and the mass spectrum standard deviation.

a. Mass spectrum mean diameter and standard deviation

The raindrop mass spectrum $m(D)$ (g mm^{-1} m^{-3}) represents the mass of liquid water as a function of raindrop diameter and is determined from the raindrop number concentration $N(D)$ by using

$$m(D) = \frac{\pi}{6\times 10^3}\rho_w N(D)D^3. \tag{13}$$

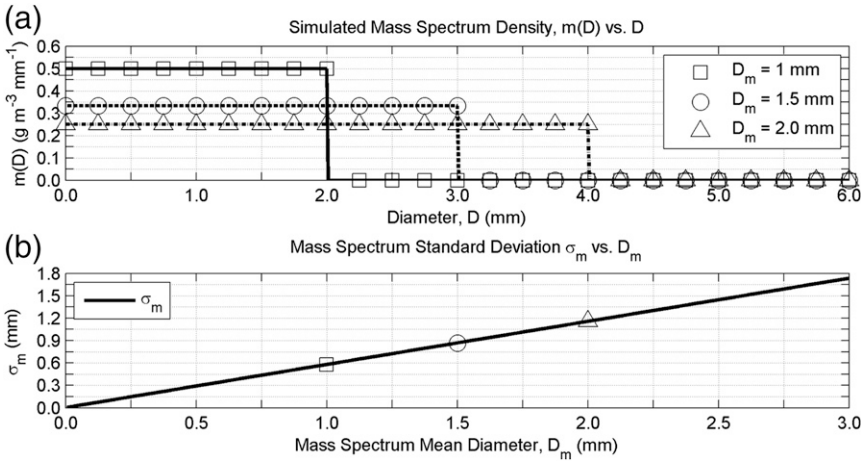

FIG. 2. Demonstration that σ_m increases as D_m increases: (a) Simulated top-hat mass spectra with $D_m = 1.0$ (squares), $D_m = 1.5$ (circles), and $D_m = 2.0$ (triangles) mm. Abscissa is raindrop diameter. (b) Calculated σ_m vs. D_m for simulated top-hat mass spectra. The symbols represent curves shown in (a), and the solid line represents the general relationship for all top-hat mass spectra with various D_m values. The abscissa is mass spectrum mean diameter D_m.

The first moment of the mass spectrum is called the mass spectrum mean diameter D_m (mm) and can be expressed by using $N(D)$ [as in Eq. (7)] or by using $m(D)$:

$$D_m = \frac{\sum_{D_{\min}}^{D_{\max}} N(D)D^4\,dD}{\sum_{D_{\min}}^{D_{\max}} N(D)D^3\,dD} = \frac{\sum_{D_{\min}}^{D_{\max}} m(D)D\,dD}{\sum_{D_{\min}}^{D_{\max}} m(D)\,dD}. \quad (14)$$

The second moment of the mass spectrum is the mass spectrum variance σ_m^2 (mm^2). The mass spectrum standard deviation σ_m (mm) is dependent on D_m and can be expressed by using $N(D)$ or $m(D)$:

$$\sigma_m = \left[\frac{\sum_{D_{\min}}^{D_{\max}} (D - D_m)^2 N(D)D^3\,dD}{\sum_{D_{\min}}^{D_{\max}} N(D)D^3\,dD}\right]^{1/2} = \left[\frac{\sum_{D_{\min}}^{D_{\max}} (D - D_m)^2 m(D)\,dD}{\sum_{D_{\min}}^{D_{\max}} m(D)\,dD}\right]^{1/2}. \quad (15)$$

The summations in Eqs. (14) and (15) extend from the minimum to the maximum observed diameters (from $D_{\min}$ to $D_{\max}$) with raindrop diameter interval dD. Since raindrops have positive diameters, the DSD is said to be "one sided," with the smallest raindrops having diameters greater than approximately 0.2 mm (Pruppacher and Klett 1978) and the largest raindrop ($D_{\max}$) observed to increase with rain-rate intensity and D_m (Ulbrich 1985). If we assume that $D_{\min}$ remains constant (near 0.2 mm) while $D_{\max}$ varies, then we would expect the mass spectrum standard deviation to increase as both D_m and $D_{\max}$ increase.

b. *Relationship between σ_m and D_m for simulated mass spectra*

To illustrate how σ_m can increase as D_m increases, Fig. 2a shows three simulated "top hat" mass spectra with constant amplitude for D = 0–2 (squares), D = 0–3 (circles), and D = 0–4 (triangles) mm. The amplitudes were arbitrarily set to 1/2, 1/3, and 1/4, respectively, to help to visualize the three distributions. From Eqs. (14) and (15), D_m and σ_m for these three distributions were 1.0, 1.5, and 2.0 mm and 0.58, 0.87, and 1.16 mm, respectively. Figure 2b shows these three pairs of D_m and σ_m values along with a line indicating a linear relationship between D_m and σ_m for mass spectra having a top-hat shape. Thus, for a general mass spectrum shape, the mass spectrum breadth increases as the mean diameter increases.

4. Disdrometer observations

To examine D_m and σ_m relationships in real data, an analysis of spectra collected using low-profile two-dimensional video disdrometers (2DVDs), manufactured

by Joanneum Research FgmbH (Graz, Austria; Schönhuber et al. 2007), was undertaken. The diameter resolution was 0.2 mm, with 50 uniformly spaced diameter bins from 0.1 to 9.9 mm. After manually verifying with ancillary observations that precipitation was rain and not snow, the first quality-control stage for each 1-min raindrop spectra consisted of retaining spectra with 1) at least 50 raindrops in at least 3 different diameter bins, 2) reflectivity factor greater than 10 dBZ, and 3) rain rate greater than 0.1 mm h^{-1}. The rain estimates were not divided by rain regime. A total of 29 705 min of raindrop spectra passed these criteria from three disdrometers deployed near Huntsville, Alabama, over an 18-month period from December 2009 to October 2011. After secondary filtering (discussed below), the number of raindrop spectra decreased to 24 872.

a. Disdrometer instrument limitations

Disdrometers count the number of raindrops passing through or hitting a surface. Because of their limited sample volume, disdrometers underestimate the number of small and large drops passing through the sample volume (Ulbrich and Atlas 1998; Kruger and Krajewski 2002). Also, wind can advect small raindrops around the instrument opening, causing the instrument to underestimate further the number of small raindrops. Nešpor et al. (2000) showed wind effects using an early version of the 2DVD, which prompted the development of the low-profile 2DVDs that were used in this study. Underestimating the small and large raindrops has an impact on estimated rain parameters (Wong and Chidambaram 1985; Chandrasekar and Bringi 1987; Smith et al. 1993, 2009; Smith and Kliche 2005) and will artificially narrow mass spectra, leading to underestimated σ_m.

To understand the impact of undercounting the number of small raindrops on σ_m estimates, a simulation was performed following the method of Moisseev and Chandrasekar (2007). In general, these simulations showed that the σ_m bias was severe for small D_m and small $D_{\max}$ and that the bias decreased as D_m and $D_{\max}$ increased. To understand whether the disdrometers were undercounting the number of small raindrops, the observed raindrop spectra were processed twice. First, σ_m was estimated using unaltered observed spectra (denoted as σ_m^{obs}). Then, the spectra were truncated to remove all number concentrations with diameters of 0.5 mm and smaller (denoted as σ_m^{trunc}). The percent change in σ_m was calculated using

$$\%\,\Delta\sigma_m = 100\frac{(\sigma_m^{\text{trunc}} - \sigma_m^{\text{obs}})}{\sigma_m^{\text{obs}}}. \tag{16}$$

A value of $\%\Delta\sigma_m = 0$ indicates that the observation was already truncated and did not observe any raindrops of 0.5 mm and smaller. Since truncated spectra are always narrower than the original spectra ($\sigma_m^{\text{trunc}} \le \sigma_m^{\text{obs}}$), truncating will always cause a negative $\%\Delta\sigma_m$.

Using 29 705 min of quality controlled observations from three side-by-side disdrometers located near Huntsville, Fig. 3a shows $\%\Delta\sigma_m$ for each 0.1-mm interval of D_m. The squares indicate the mean, and the lines show ± 1 standard deviation. For D_m greater than 1 mm, the mean $\%\Delta\sigma_m$ is less than 10%, indicating that truncation will have a small impact on σ_m. For D_m less than 1 mm, however, the mean $\%\Delta\sigma_m$ has a very large magnitude, indicating that truncation significantly narrows the spectra causing σ_m to decrease. This sensitivity to small-drop truncation when D_m is less than 1 mm indicates that the disdrometers are observing some small raindrops. But without independent observations, it is difficult to determine whether wind effects and instrument limitations are reducing the number of detected small drops relative to the unknown true population. To avoid using potentially biased σ_m estimates in power-law calculations in section 5, all power-law calculations are performed using only estimates with $D_m > 1$ mm. The power-law relations are then extrapolated into the $D_m \le 1$ mm range.

Figure 3b shows the normalized maximum diameter $X_{\max} = D_{\max}/D_m$ for each 0.1-mm interval of D_m. Since our Moisseev and Chandrasekar (2007) method simulations indicated that σ_m biases decrease as $X_{\max}$ increases (not shown), all observations with $X_{\max} \le 1.5$ were filtered from the dataset. Approximately 84% (24 872 min) of the original Huntsville observations had $X_{\max} > 1.5$ and were used for further analysis.

b. Observed 2D distributions

Using 24 872 min of filtered Huntsville raindrop spectra (see previous section for the filtering procedure), Fig. 4 shows the frequency of occurrence of reflectivity factor Z (dBZ), rain rate as $10\log_{10}(R)$ (dBR), and σ_m as a function of D_m. The pixel with the most occurrences in each panel is normalized to have 0 dB. Each 50% decrease in occurrence has a 3-dB decrease on the logarithmic color scale. Table 1 lists the Pearson correlation coefficients between reflectivity Z_e (mm^6 m^{-3}), rain rate R (mm h^{-1}), D_m, and σ_m.

Using observations with $D_m > 1.0$ mm (a total of 18 969 observations), power-law curves are estimated with the form $y = aD_m^b$ (where $y = Z_e$, R, or σ_m) and are shown in Fig. 4 with solid lines ($D_m > 1.0$ mm) and dashed lines ($D_m \le 1.0$ mm). The power-law coefficients and exponents were determined using the correlation

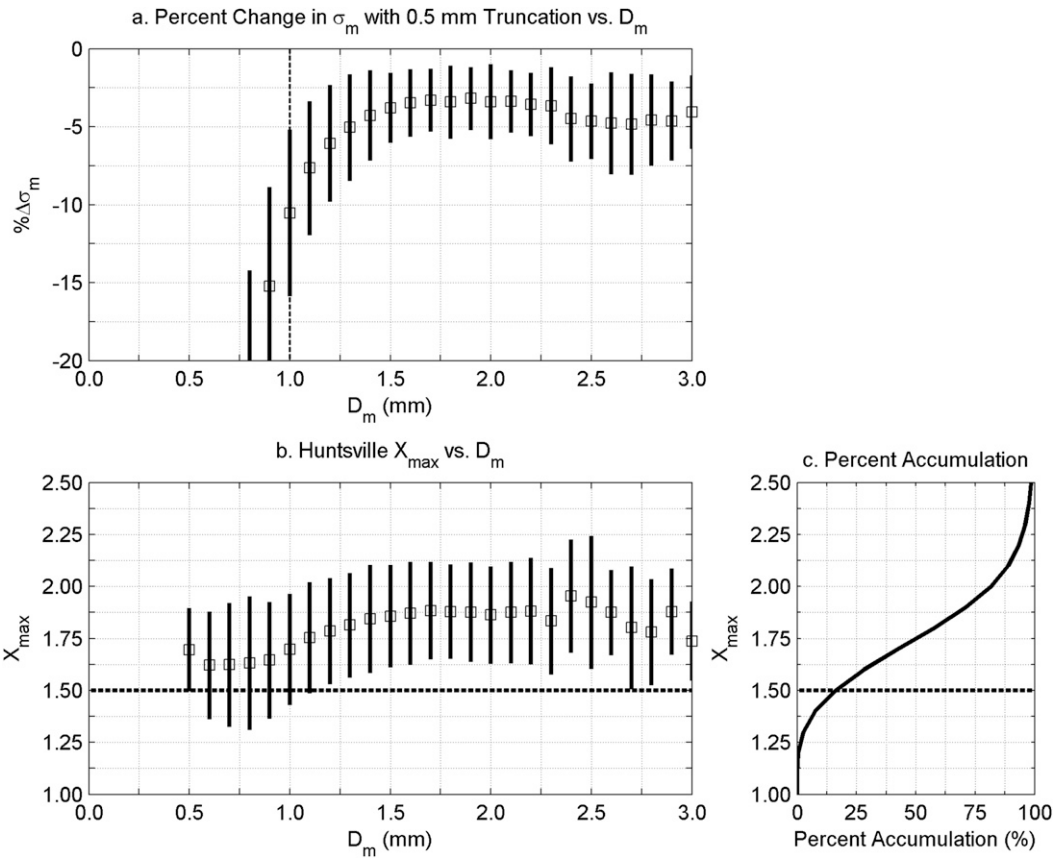

FIG. 3. Sensitivity of estimated σ_m to truncated spectra: (a) Percent change in σ_m between the observed and truncated spectra estimated for 0.1-mm intervals of D_m. Squares represent the mean, and lines span over the mean ± one standard deviation (STD). All raindrops 0.5 mm and smaller are removed from spectra before calculating truncated σ_m. (b) The mean (squares) and mean ± STD (lines) of normalized maximum observed diameter $X_{\max} = D_{\max}/D_m$ for 0.1-mm intervals of D_m. The dashed line indicates the threshold used to filter narrow spectra. (c) Percent accumulation of observations as a function of $X_{\max}$. Approximately 16% of the observations had $X_{\max} < 1.5$, leaving 84% (24 872 min) of observations available for further analysis.

method described in Haddad et al. (1996) and also described in section 5.

c. D_m–σ_m–μ relationships for gamma-shaped DSDs

The σ_m and D_m estimates in Fig. 4c were calculated directly from the disdrometer spectra using Eqs. (14) and (15) and do not assume a gamma-shaped DSD. As discussed in the introduction, there are mathematical relationships between D_m, σ_m, and μ for gamma-shaped DSDs (Ulbrich 1983; Ulbrich and Atlas 1998; Bringi and Chandrasekar 2001). These mathematical relationships are derived in this section to define a mapping from DSD physical attributes (D_m and σ_m) to gamma function parameters (D_m and μ).

The mass spectrum standard deviation for a gamma-shaped DSD $\sigma_{m,\mathrm{gamma}}$ (the subscript "gamma" indicates a gamma function) is a function of D_m and μ and is determined by substituting Eqs. (3) and (5) into Eq. (15) to yield

$$\sigma_{m,\mathrm{gamma}}(D_m,\mu) = \left\{ \frac{\sum_{D_{\min}}^{D_{\max}} (D - D_m)^2 \left(\frac{D}{D_m}\right)^{\mu+3} \exp\left[-(4+\mu)\left(\frac{D}{D_m}\right)\right] dD}{\sum_{D_{\min}}^{D_{\max}} \left(\frac{D}{D_m}\right)^{\mu+3} \exp\left[-(4+\mu)\left(\frac{D}{D_m}\right)\right] dD} \right\}^{1/2}. \tag{17}$$

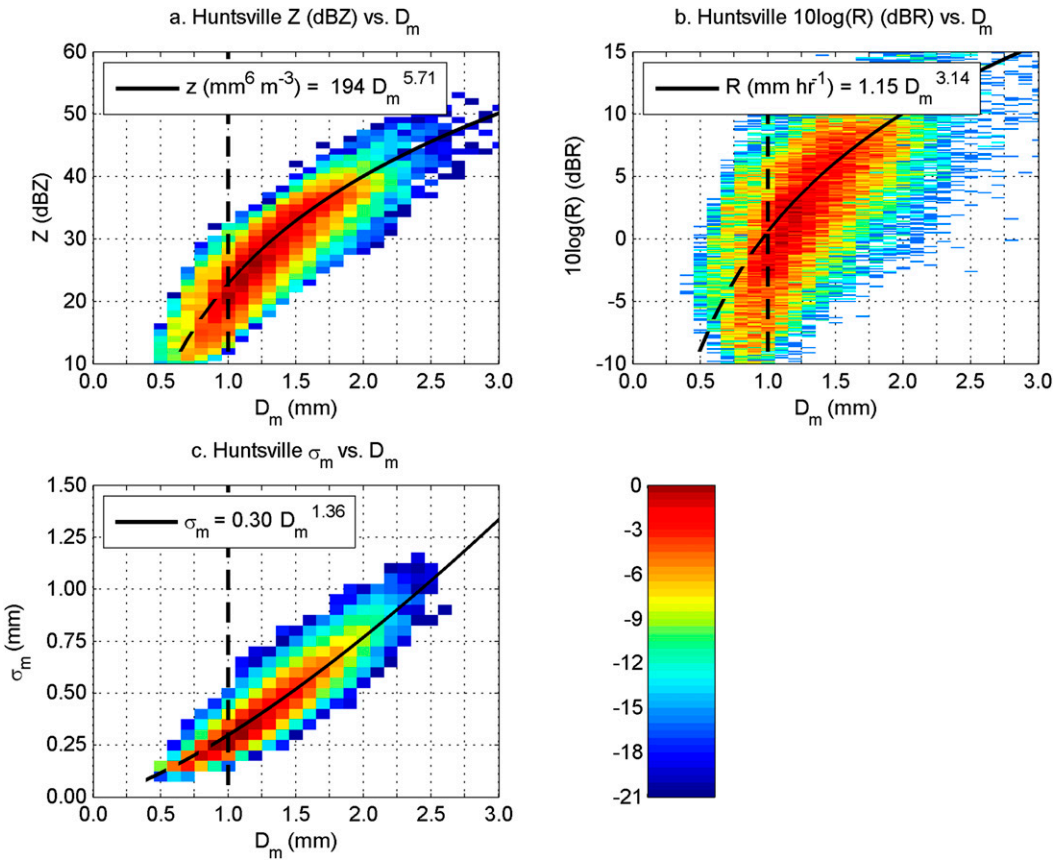

FIG. 4. Demonstration that Z, R, and σ_m are correlated with D_m: frequency of occurrence from 24 872 min of 2DVD observations from Huntsville of (a) Z (dBZ) (b) R (dBR), and (c) σ_m vs D_m (color tiles; scale is logarithmic defined such that the pixel with the most occurrences has 0 dB and each 50% decrease in occurrence has a 3-dB decrease on the color scale). The solid black lines in (a)–(c) are power-law curves given by the equations in the labels.

With an assumption that $D_{\min} = 0$, $D_{\max} = \infty$, and $dD \to 0$, Eq. (17) simplifies to (Ulbrich 1983; Ulbrich and Atlas 1998)

$$\sigma_{m,\mathrm{gamma}}(D_m, \mu) = D_m/(4+\mu)^{1/2}. \tag{18}$$

To illustrate the relationship of Eq. (18), Fig. 5a shows σ_m versus D_m frequency of occurrence shown in Fig. 4c along with $\sigma_{m,\mathrm{gamma}}$ for constant μ values of 0 (squares), 3 (circles), 5 (triangles), and 10 (inverted triangles). The derived power-law curves are shown with dashed lines ($D_m \le 1.0$ mm) and solid lines ($D_m > 1.0$ mm) and pass through the constant $\mu = 10$ inverted triangles and $\mu = 5$ triangles near $D_m = 0.7$ and 1.3 mm, respectively. The normalized σ_m PDF is shown in Fig. 5b. As a reference, the Zhang et al. (2003) μ–Λ relationship in Eq. (2) is shown in Fig. 5a (blue solid line) after converting Eq. (2) to a σ_m–D_m relationship using Eq. (17) and

$$D_m = (4+\mu)/\Lambda. \tag{19}$$

There are three important points to glean from Fig. 5a. First, since σ_m and D_m were estimated without assuming a gamma-shaped DSD and the gamma DSD $\sigma_{m,\mathrm{gamma}}$ function with μ ranging from 0 to 10 bounds the observed distribution of σ_m versus D_m, we can conclude that a family of gamma functions can describe the shape of the observed DSDs. Second, the Zhang et al. (2003) μ–Λ relationship passes through the σ_m–D_m distribution for $D_m < 2.0$ mm. Third, the σ_m PDF shown in Fig. 5b is

TABLE 1. Pearson correlation coefficients between rain parameters estimated from 24 872 min of filtered Huntsville disdrometer observations. Correlation coefficients are between reflectivity Z_e (mm^6 m^{-3}), rain rate R (mm h^{-1}), mean mass spectrum diameter D_m (mm), mass spectrum standard deviation σ_m (mm), and normalized mass spectrum standard deviation σ'_m (unitless).

	R	D_m	σ_m	σ'_m
Z_e	0.85	0.47	0.45	−0.01
R	—	0.52	0.47	−0.04
D_m	—	—	0.91	0.01
σ_m	—	—	—	0.38

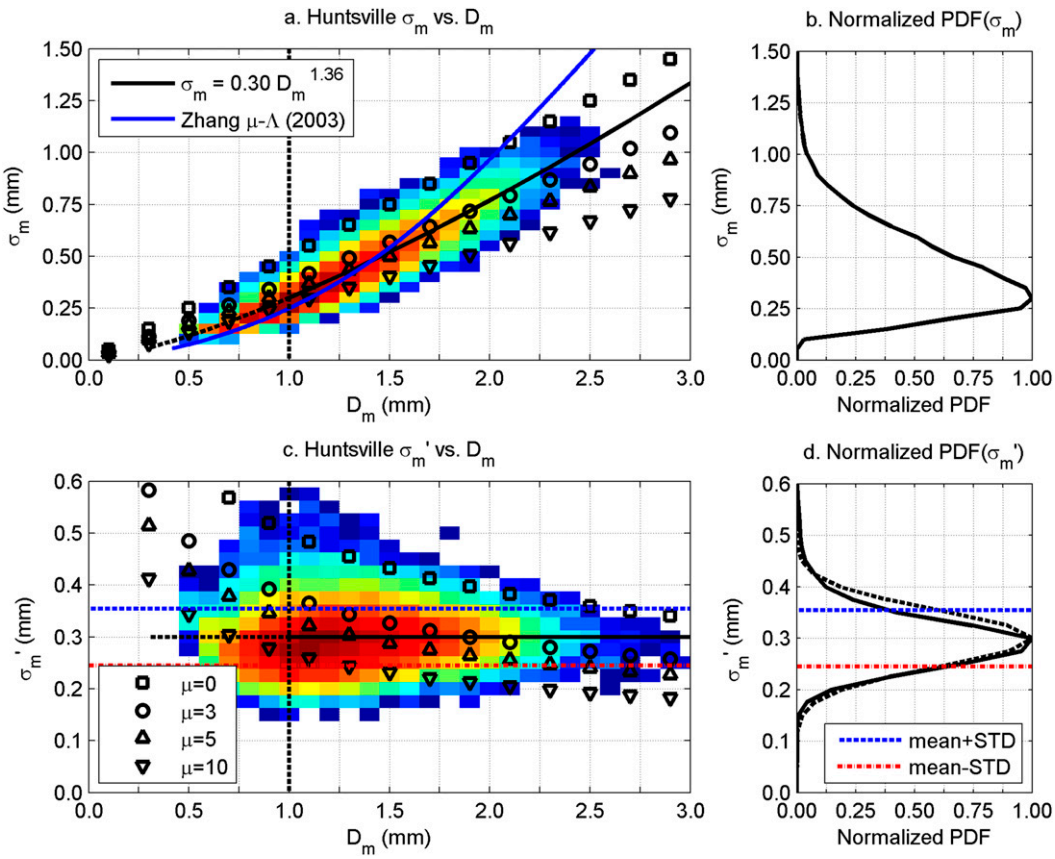

FIG. 5. Demonstration that weighting σ_m with $D_m^{1.36}$ provides a variable σ'_m that is uncorrelated with D_m: (a) Frequency of occurrence of σ_m vs D_m (same as Fig. 4c). The black solid line is the power-law fit (same as Fig. 4c), and the blue line is the Zhang et al. (2003) μ–Λ relationship mapped into σ_m vs. D_m. (b) The σ_m PDF normalized such that maximum occurrence is unity. (c) Frequency of occurrence of σ'_m vs D_m. (d) Two normalized PDFs. The solid black line is the observed normalized σ'_m PDF with $\overline{\sigma'_m} = 0.30$ and STD $\mathrm{std}(\sigma'_m) = 0.058$. The dashed black line is a normalized Gaussian curve with the same mean and STD. Dashed blue and red lines are mean + STD and mean − STD, respectively. In (a) and (c), symbols represent constant μ values of 0 (squares), 3 (circles), 5 (triangles), and 10 (inverted triangles) and the color scale is the same as in Fig. 4.

asymmetric and indicates it would be difficult to use σ_m directly in probabilistic retrieval algorithms that assume that parameters are Gaussian distributed.

Note that Eq. (18) is a simple mathematical relationship between D_m, σ_m, and μ and was determined after "mathematically" forcing raindrop diameters to extend from $D_{\min} = 0$ to $D_{\max} = \infty$. Equation (18) does not account for any small-drop truncation in observed disdrometer raindrop spectra as discussed in section 4a. Also, Eq. (18) does not account for finite maximum diameter, $D_{\max} < \infty$. Both topics need to be addressed in future work.

5. Statistically independent DSD shape attributes

Figure 4 shows frequency of occurrence of Z, R, and σ_m as a function of D_m. The largest correlation coefficient is between D_m and σ_m (see Table 1) and indicates that these two DSD shape attributes are not independent. Developing constraints using D_m and σ_m will be subject to mathematical artifacts similar to μ–Λ relationships. To avoid potential mathematical artifacts, DSD relationships need to be developed using statistically independent shape attributes. This section uses the method described by Haddad et al. (1996) to construct a new mass spectrum standard deviation that is statistically independent of D_m.

a. Statistically independent DSD shape attributes

To construct a new mass spectrum standard deviation σ'_m that is independent of D_m, Haddad et al. (1996) proposed a power-law transformation of the form

$$\sigma'_m = \sigma_m / D_m^{b_m} . \tag{20}$$

To make σ'_m and D_m statistically independent, the exponent b_m is adjusted until the Pearson correlation

coefficient between σ'_m and D_m is zero (Haddad et al. 1996).

Using the 18 969 disdrometer observations with $D_m >$ 1.0 mm, a zero correlation coefficient occurred when $b_m = 1.36$. This is the exponent shown in the power-law curves in Fig. 4c. Using σ_m and D_m estimated for each disdrometer observation, σ'_m is determined using Eq. (20) and $b_m = 1.36$ with the two-dimensional frequency of occurrence shown in Fig. 5c. The normalized σ'_m PDF is shown in Fig. 5d.

The mean σ'_m (denoted as $\overline{\sigma'_m}$) and σ'_m standard deviation [denoted as std(σ'_m)] had values of 0.30 and 0.058, respectively. Figure 5d shows the normalized σ'_m PDF (solid black line) and a normalized Gaussian curve with the same mean and standard deviation (dashed black lines). The observed and Gaussian σ'_m PDF curves are very similar suggesting that σ'_m distributions can be described using Gaussian statistics and can be used in probabilistic retrieval algorithms. The upper bound $\overline{\sigma'_m}$ + std(σ'_m) (blue dashed line) and lower bound $\overline{\sigma'_m}$ − std(σ'_m) (red dash–dotted line) are shown in Fig. 5c with 55% of the observed σ'_m within these two bounds. For reference, $\sigma_{m,\mathrm{gamma}}$ for constant μ values of 0 (squares), 3 (circles), 5 (triangles), and 10 (inverted triangles) is also shown in Fig. 5c.

One way to interpret Fig. 5c is to consider it as joint PDF plots of D_m and σ'_m. For each possible value of D_m, the breadth of the DSD is described by σ'_m. Since σ'_m was constructed to be statistically independent of D_m, the most likely, or expected, value of σ'_m is given by $\overline{\sigma'_m}$. And the spread of possible breadth values is Gaussian shaped with standard deviation of std(σ'_m).

It is now possible to describe D_m and σ_m as joint PDFs by rearranging Eq. (20) to yield

$$\sigma_m = \sigma'_m D_m^{b_m}. \tag{21}$$

For each value of D_m, the most likely, or expected, σ_m value is given by

$$\sigma_m^{\mathrm{expected_value}} = \overline{\sigma'_m} D_m^{b_m} = 0.30 D_m^{1.36}. \tag{22}$$

And the upper bound and lower bounds of σ_m that capture 55% of the observations are given by

$$\sigma_m^{\mathrm{upper_bound}} = [\overline{\sigma'_m} + \mathrm{std}(\sigma'_m)] D_m^{b_m} = 0.358 D_m^{1.36} \quad \text{and} \tag{23}$$

$$\sigma_m^{\mathrm{lower_bound}} = [\overline{\sigma'_m} - \mathrm{std}(\sigma'_m)] D_m^{b_m} = 0.242 D_m^{1.36}. \tag{24}$$

To visualize the D_m and σ_m as joint PDFs, the σ_m frequency of occurrence is shown in Fig. 6a along with the expected value, lower bound, and upper bound for each value of D_m. Note that the breadth of σ_m, centered on the expected value, increases as D_m increases.

b. *Transformation from physical attributes to gamma parameters*

The new mass spectrum standard deviation σ'_m is defined without assuming the DSD follows a gamma distribution, but if an algorithm assumes that the DSD follows a gamma distribution then each (D_m, σ'_m) pair can be transformed into a (D_m, μ) pair using Eqs. (18) and (21) to obtain

$$\mu = \frac{D_m^{2-2b_m}}{\sigma'^2_m} - 4. \tag{25}$$

Each of the 24 872 disdrometer σ'_m estimates are transformed into μ estimates using Eq. (25) and are shown in Fig. 6c as a frequency of occurrence plot. The normalized μ PDF is shown in Fig. 6d (black solid line) along with a normalized Gaussian curve (black dashed line) constructed with the same $\overline{\mu} = 6.9$ and std(μ) = 5.1. The normalized μ PDF does not follow a Gaussian shape, but is an asymmetric distribution with a peak near $\mu = 4$.

Similar to interpreting Fig. 6a as a joint PDF plot of D_m and σ_m, Fig. 6c can be considered a joint PDF plot of D_m and μ. For each possible D_m, the expected μ value is given by Eq. (25) with σ'_m replaced with $\overline{\sigma'_m} = 0.30$ and $b_m = 1.36$:

$$\mu^{\mathrm{expected}} = \frac{D_m^{2-2b_m}}{\sigma'^2_m} - 4 = \frac{D_m^{-0.72}}{0.09} - 4 = 11.1 D_m^{-0.72} - 4. \tag{26}$$

The lower and upper μ bounds containing 55% of the observations are given by Eq. (25) with σ'_m replaced with $\overline{\sigma'_m}$ + std(σ'_m) and $\overline{\sigma'_m}$ − std(σ'_m), respectively. The expected μ value, lower bound, and upper bound are shown in Fig. 6c. With this joint PDF interpretation, Fig. 6c indicates that the expected value and breadth of possible μ values decrease as D_m increases.

6. Estimated rain rate using μ constraints

This section uses the simple DPR rain-rate retrieval algorithm developed in section 2 to evaluate whether more accurate rain rates occur if μ is held constant or if it is described as a function of D_m. Six different rain-rate estimates are produced using the same observed disdrometer reflectivity Z_e^{disd} (mm^6 m^{-3}) and D_m^{disd} (mm) but using six different μ values. Four models used a constant μ of 0, 3, 5, and 10. The other two models

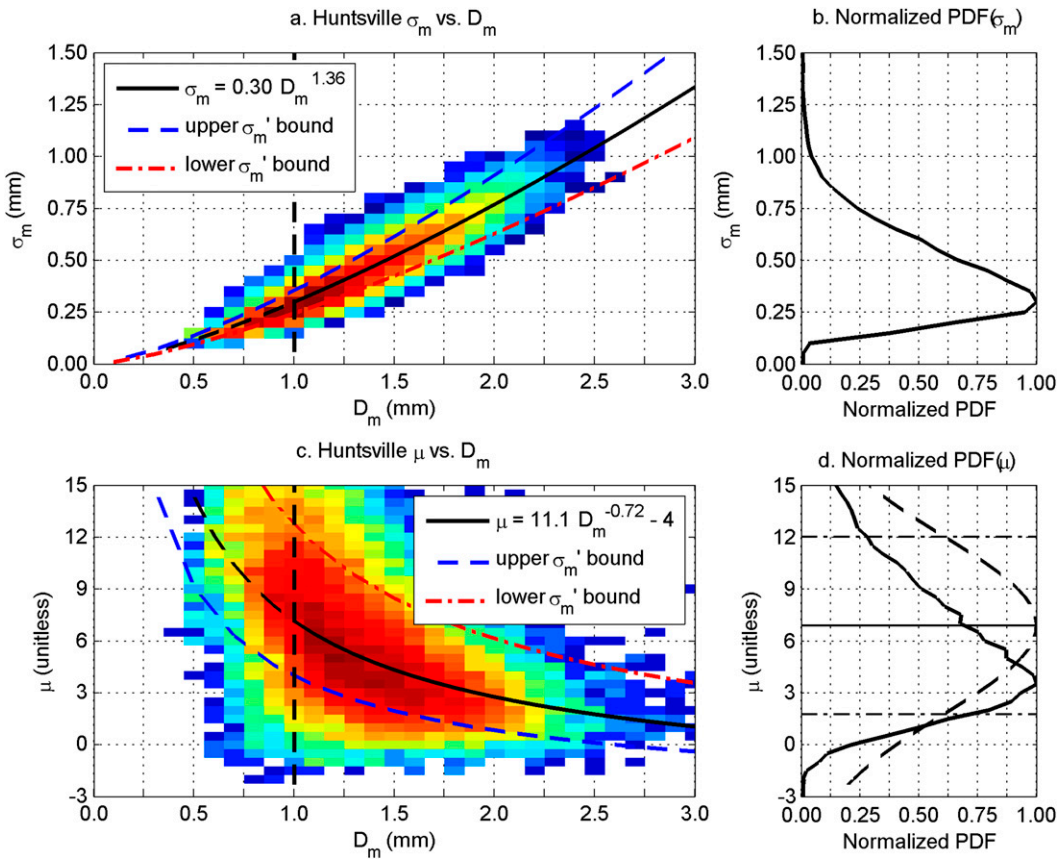

FIG. 6. Mapping from (D_m, σ_m) space to (D_m, μ) space: (a) Frequency of occurrence of σ_m vs D_m (same as Figs. 4c and 5a); black solid line is power-law fit (same as Figs. 4c and 5a), and blue dashed and red dash–dotted lines represent upper and lower σ'_m bounds, respectively. (b) Normalized σ_m PDF. (c) Frequency of occurrence of μ vs D_m; blue dashed and red dash–dotted lines represent upper and lower σ'_m bounds, respectively. (d) Two normalized PDFs. The solid line is the normalized μ PDF with mean $\overline{\mu} = 6.9$ and std$(\mu) = 5.1$. The dashed black line is a normalized Gaussian curve with $\overline{\mu} = 6.9$ and std$(\mu) = 5.1$. Black dash–dotted lines are $\overline{\mu} \pm$ std(μ). In (a) and (c), the color scale is the same as in Fig. 4.

expressed μ as a function of D_m: one model used the expected μ value from Eq. (26) and the other model used a μ derived from the Zhang et al. (2003) μ–Λ constraint presented in Eq. (2).

Following the logic of the simple DPR rain algorithm in section 2, the normalized number concentration $N_w^{\mathrm{disd}}(\mu_i)$ is estimated for each μ_i ($i = 1, \ldots, 6$) using the observed Z_e^{disd} and D_m^{disd} estimates and

$$N_w^{\mathrm{disd}}(\mu_i) = \frac{Z_e^{\mathrm{disd}}}{\dfrac{6}{4^4}\dfrac{(4+\mu_i)^{\mu_i+4}}{\Gamma(\mu_i+4)}\displaystyle\sum_{D_{\min}}^{D_{\max}}\left(\frac{D}{D_m^{\mathrm{disd}}}\right)^{\mu_i}\exp\left[-(4+\mu_i)\left(\frac{D}{D_m^{\mathrm{disd}}}\right)\right]D^6\,dD}. \tag{27}$$

Following the format of Eq. (12), six model rain rates are estimated using

$$R_{\mathrm{model}}(\mu_i) = \frac{6\pi}{10^3}\sum_{D_{\min}}^{D_{\max}} N_w^{\mathrm{disd}}(\mu_i) f(D; D_m^{\mathrm{disd}}, \mu_i) D^3 v(D)\,dD. \tag{28}$$

The observed rain rate is derived from the observed discrete number concentration $N_{obs}^{\mathrm{disd}}(D)$ by using

$$R_{\mathrm{obs}} = \frac{6\pi}{10^3}\sum_{D_{\min}}^{D_{\max}} N_{\mathrm{obs}}^{\mathrm{disd}}(D) D^3 v(D)\,dD. \tag{29}$$

The same raindrop fall speed relationship $v(D)$ is used for both $R_{\mathrm{model}}(\mu_i)$ and R_{obs}. One difference in calculating

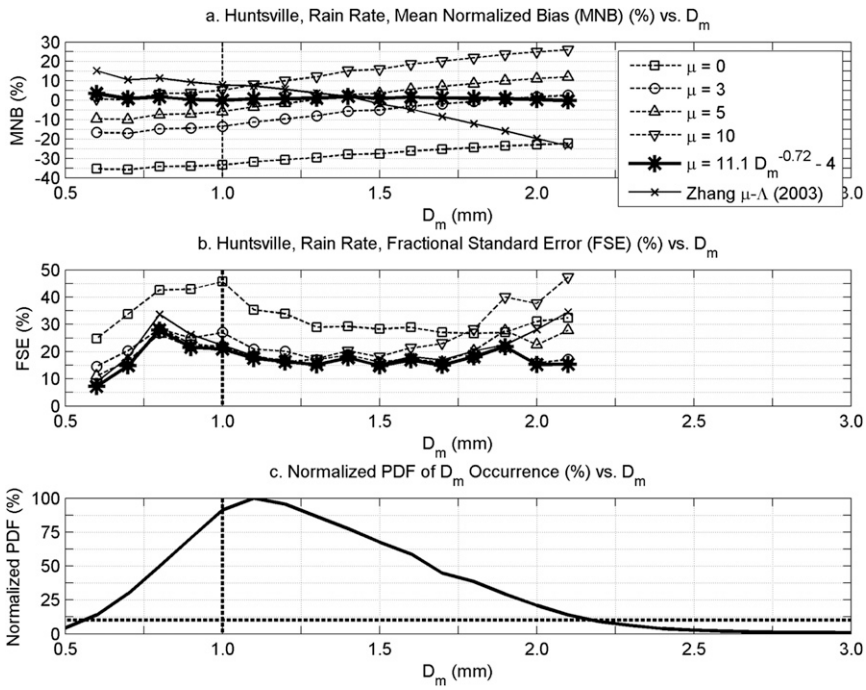

FIG. 7. Demonstration that the $\sigma'_m - D_m - \mu$ constraint in rainfall algorithm has smaller mean normalized bias than a constant μ constraint: (a) MNB (%) and (b) FSE (%) for rain rate estimated with the six different μ assumptions that are listed in (a). (c) The normalized frequency of occurrence as a function of D_m. The dashed line at 10% indicates the threshold for evaluating model results.

the two rain-rate estimates is that the summation limits extend from 0.1 to 9.9 mm for $R_{\text{model}}(\mu_i)$ and from the observed $D_{\min}$ to $D_{\max}$ for R_{obs}.

The observations are divided into small intervals of D_m. For each 0.1-mm D_m interval, the mean normalized bias (MNB) and fractional standard error (FSE) (both expressed as a percent) between R_{model} and R_{obs} are estimated by using

$$\text{MNB}\,(\%) = \frac{100}{n}\sum_{j=1}^{n}\frac{[R_{\text{model}}(j) - R_{\text{obs}}(j)]}{R_{\text{obs}}(j)} \quad \text{and} \tag{30}$$

$$\text{FSE}\,(\%) = 100\frac{\text{std}(R_{\text{model}} - R_{\text{obs}})}{\overline{R}_{\text{obs}}}, \tag{31}$$

with j representing the samples within each interval. Figures 7a and 7b show the MNB and FSE for each model as a function of D_m. Figure 7c shows the occurrence versus D_m. The constant μ models have similar-shaped MNB curves that increase in value with increasing D_m. The $\mu = 0$ model has the most negative bias, with MNB ranging from −35% to −20%. The $\mu = 10$ model has the most positive bias, with MNB ranging from 0% to 25%. The model using the Zhang et al. (2003) μ–Λ constraint has a positive bias for D_m of less than 1.25 mm but makes a transition to a negative bias for larger D_m. The power-law $\mu^{\text{expected}} = 11.1D_m^{-0.72} - 4$ constraint has the smallest bias, with MNB never exceeding 3.5% in magnitude.

Except for the $\mu = 0$ model, the FSE for all models is nearly the same, with an average of 20% ± 4% (the $\mu = 0$ model average is 32%). Table 2 lists the MNB and FSE for the six models at D_m of 1.0, 1.5, and 2.0 mm. The large FSE for all models reflects the simplicity of the rain-rate retrieval algorithm. All models represent the DSD with just one μ value for each D_m. An algorithm that varies μ on the basis of additional information will reduce the FSE.

7. Conclusions

The dual-frequency precipitation radar planned for the core satellite of the Global Precipitation Measurement mission will provide dual-frequency reflectivity measurements of precipitation. Rainfall retrieval algorithms will assume a gamma raindrop size distribution with three mathematical parameters N_w, D_m, and μ. One challenge for the DPR retrieval algorithm is to estimate rainfall that is modeled with three DSD parameters using only two radar measurements. This underconstrained problem requires the algorithm to assume that

TABLE 2. MNB and FSE for modeled rain-rate estimates at selected D_m and six different values of μ. The number of samples in each 0.1-mm interval is labeled as n.

	$D_m = 1.0 \pm 0.05$ (mm; $n = 2455$)		$D_m = 1.5 \pm 0.05$ (mm; $n = 1822$)		$D_m = 2.0 \pm 0.05$ (mm; $n = 565$)	
μ	MNB (%)	FSE (%)	MNB (%)	FSE (%)	MNB (%)	FSE (%)
0	−33	46	−28	28	−23	31
3	−13	27	−5.1	16	1.7	16
5	−5.8	22	3.5	15	11	23
10	5.2	21	16	18	25	38
$11.1D_m^{-0.72} - 4$	−0.1	21	1.0	15	0.3	15
Zhang et al. (2003) μ–Λ	7.9	22	−1.9	15	−20	28

one parameter is a constant or a function of another parameter. Since GPM rainfall algorithms will use either optimal estimation theory (Munchak and Kummerow 2011) or Bayesian theory (Haddad et al. 2006) to form probabilistic algorithms, the DSD constraint needs to have an initial (or expected) value *plus* an acceptable range of values. The acceptable range of values allows the algorithm to deviate from the expected value as dictated by the observations.

One option is to constrain the DSD parameters with a μ–Λ constraint (Zhang et al. 2003), but μ–Λ constraints only provide an expected value and do not provide a range of values allowing probabilistic algorithms to deviate from the expected value. Also, since μ and Λ represent mathematical parameters of a gamma function they are highly correlated and thus μ–Λ relationships may contain mathematical artifacts (Chandrasekar and Bringi 1987; Moisseev and Chandrasekar 2007). To avoid these mathematical artifacts, relationships need to be developed before assuming the DSD follows any particular mathematical shape.

This study analyzed over 20 000 minutes of surface disdrometer raindrop mass spectra and found that the mean diameter D_m and mass spectrum standard deviation σ_m were highly correlated ($r^2 = 0.91$). This high correlation may lead to mathematical artifacts in DSD constraints based on σ_m–D_m relationships. To avoid mathematical artifacts, a new breadth variable σ'_m is defined and constructed to be statistically independent of D_m. This new breadth variable is nearly Gaussian distributed and thus is well suited for probabilistic algorithms, with the mean value $(\overline{\sigma'_m})$ representing the expected value and $\mathrm{std}(\sigma'_m)$ representing a dispersion of possible breadth values.

Since σ'_m is independent of D_m and is determined without assuming a DSD shape, σ'_m and D_m represent two moments of the DSD mass spectrum. For algorithms that assume gamma-shaped DSDs with D_m and μ parameters, there is a mapping from (D_m, σ'_m) space to (D_m, μ) space with joint PDFs describing the expected value and range of μ for each D_m. For a disdrometer dataset collected in Huntsville, the $\sigma'_m - D_m - \mu$ mapping yielded a power-law expected μ value of the form $\mu^{\text{expected}} = 11.1D_m^{-0.72} - 4$. One benefit of using a $\sigma'_m - D_m - \mu$ constraint is that rainfall estimates have smaller biases than assuming a constant μ constraint. Using a simple rainfall algorithm, the expected value $\sigma'_m - D_m - \mu$ constraint had a mean normalized bias of less than 3.5%, whereas all constant μ constraints had biases over 20%.

This analysis used disdrometer observations to develop DSD constraints that provide initial values and ranges of acceptable values for underconstrained probabilistic rainfall algorithms. Without any other information, an algorithm can start at the initial value and then use observations and algorithm logic to deviate from this initial value. This analysis provides a statistical representation of DSD parameter assumptions that can be incorporated into algorithm logic. For completeness, note that power-law DSD constraints developed in this analysis should not be used to estimate DSD parameters in disdrometer datasets. The DSD constraints are statistical representations of DSD physical attributes or DSD parameters and do not represent instantaneous values estimated from individual DSD spectra.

There are topics of this study that need further research. First of all, if surface disdrometers underestimate the number of small raindrops, then the mass spectrum will be too narrow and σ_m will be negatively biased. The σ_m bias that is due to small raindrop truncation is a function of D_m, with the biases decreasing with increasing D_m. To avoid potential σ_m biases, this study used σ_m when D_m was greater than 1.0 mm. Since this work focused on developing joint PDFs of D_m and σ_m, the impacts of small-drop truncation may be within the upper and lower bounds (or other statistics) of the joint PDFs. Future work needs to address if and how often surface disdrometers underestimate the number of small raindrops in rain, including the raindrops that are advected around the instrument. Future work should also aim to

understand how undercounting the number of small raindrops affects joint PDFs derived from observed physical attributes of the DSD.

The maximum observed raindrop diameter $D_{\max}$ affects the calculated mass spectrum breadth and also has an impact on the mapping of physical attributes in (D_m, σ'_m) space into gamma parameters in (D_m, μ) space. The mapping assumed that raindrops ranged in size from $D_{\min} = 0$ to $D_{\max} = \infty$, allowing the use of complete gamma functions in deriving Eq. (18). Work is needed to determine how the range of observed raindrop sizes, from $D_{\min} > 0$ to $D_{\max} < \infty$, affects the mapping of physical attributes into gamma parameters.

Another topic that needs further investigation is the site-to-site and rain regime-to-regime variability of the power-law relationship that causes D_m and σ'_m to be statistically independent. The data used in this study were from one site and were not divided by rain regime. Investigations of the cloud physics mechanisms that may be regionally dependent and lead to variations in these statistical relationships will be critical for global rainfall estimation.

Shifts in σ'_m from the mean value $\overline{\sigma'_m}$ are reflective of different microphysical processes. Deviations of σ'_m from $\overline{\sigma'_m}$ indicate narrower ($\sigma'_m < \overline{\sigma'_m}$) or broader ($\sigma'_m > \overline{\sigma'_m}$) spectra. It is plausible that cloud processes (such as convective vs stratiform rain) and meteorological regimes lead to shifts in these relationships.

Acknowledgments. Support for this work was provided by Ramesh Kakar under the NASA Precipitation Measurement Missions (PMM) and NASA Global Precipitation Measurement (GPM) mission, including Grants NNX13AI94G, NNX10AM54G, NNX13AF89G, NNX12AD03A, NNX10AP84G, NNX13AF86G, NNX13AJ55G, NNX13AI89G, and NNX10AH66G. The authors thank Dr. Merhala Thurai for her insightful discussions.

REFERENCES

Atlas, D., and C. Ulbrich, 2006: Drop size spectra and integral remote sensing parameters in the transition from convective to stratiform rain. *Geophys. Res. Lett.,* **33,** L16803, doi:10.1029/2006GL026824.

Bringi, V. N., and V. Chandrasekar, 2001: *Polarimetric Doppler Weather Radar: Principles and Applications.* Cambridge University Press, 636 pp.

——, ——, J. Hubbert, E. Gorgucci, W. L. Randeu, and M. Schoenhuber, 2003: Raindrop size distribution in different climatic regimes from disdrometer and dual-polarized radar analysis. *J. Atmos. Sci.,* **60,** 354–365, doi:10.1175/1520-0469(2003)060<0354:RSDIDC>2.0.CO;2.

Cao, Q., and G. Zhang, 2009: Errors in estimating raindrop size distribution parameters employing disdrometer and simulated raindrop spectra. *J. Appl. Meteor. Climatol.,* **48,** 406–425, doi:10.1175/2008JAMC2026.1.

——, ——, E. A. Brandes, T. Schuur, A. Ryzhkov, and K. Ikeda, 2008: Analysis of video disdrometer and polarimetric radar data to characterize rain microphysics in Oklahoma. *J. Appl. Meteor. Climatol.,* **47,** 2238–2255, doi:10.1175/2008JAMC1732.1.

Chandrasekar, V., and V. N. Bringi, 1987: Simulation of radar reflectivity and surface measurements of rainfall. *J. Atmos. Oceanic Technol.,* **4,** 464–478, doi:10.1175/1520-0426(1987)004<0464:SORRAS>2.0.CO;2.

——, W. Li, and B. Zafar, 2005: Estimation of raindrop size distribution from spaceborne radar observations. *IEEE Trans. Geosci. Remote Sens.,* **43,** 1078–1086, doi:10.1109/TGRS.2005.846130.

Grecu, M., L. Tian, W. S. Olson, and S. Tanelli, 2011: A robust dual-frequency radar profiling algorithm. *J. Appl. Meteor. Climatol.,* **50,** 1543–1557, doi:10.1175/2011JAMC2655.1.

Haddad, Z. S., S. L. Durden, and E. Im, 1996: Parameterizing the raindrop size distribution. *J. Appl. Meteor.,* **35,** 3–13, doi:10.1175/1520-0450(1996)035<0003:PTRSD>2.0.CO;2.

——, J. P. Meagher, S. L. Durden, E. A. Smith, and E. Im, 2006: Drop size ambiguities in the retrieval of precipitation profiles from dual-frequency radar measurements. *J. Atmos. Sci.,* **63,** 204–217, doi:10.1175/JAS3589.1.

Hou, A. Y., G. Skofronick-Jackson, C. D. Kummerow, and J. M. Shepherd, 2008: Global precipitation measurement. *Precipitation: Advances in Measurement, Estimation and Prediction,* S. C. Michaelides, Ed., Springer, 131–170.

Huffman, G. J., and Coauthors, 2007: The TRMM multi-satellite precipitation analysis (TMPA): Quasi-global, multiyear, combined-sensor precipitation estimates at fine scales. *J. Hydrometeor.,* **8,** 38–55, doi:10.1175/JHM560.1.

Iguchi, T., T. Kozu, J. Kwiatkowski, R. Meneghini, J. Awaka, and K. Okamoto, 2009: Uncertainties in the rain profiling algorithm for the TRMM precipitation radar. *J. Meteor. Soc. Japan,* **87A,** 1–30, doi:10.2151/jmsj.87A.1.

Illingworth, A. J., and T. M. Blackman, 2002: The need to represent raindrop size spectra as normalized gamma distributions for the interpretation of polarization radar observations. *J. Appl. Meteor.,* **41,** 286–297, doi:10.1175/1520-0450(2002)041<0286:TNTRRS>2.0.CO;2.

Kozu, T., T. Iguchi, T. Kubota, N. Yoshida, S. Seto, J. Kwiatkowski, and Y. Takayabu, 2009: Feasibility of raindrop size distribution parameter estimation with TRMM precipitation radar. *J. Meteor. Soc. Japan,* **87A,** 53–66, doi:10.2151/jmsj.87A.53.

Kruger, A., and W. F. Krajewski, 2002: Two-dimensional video disdrometer: A description. *J. Atmos. Oceanic Technol.,* **19,** 602–617, doi:10.1175/1520-0426(2002)019<0602:TDVDAD>2.0.CO;2.

Kummerow, C. D., S. Ringerud, J. Crook, D. Randel, and W. Berg, 2011: An observationally generated a priori database for microwave rainfall retrievals. *J. Atmos. Oceanic Technol.,* **28,** 113–130, doi:10.1175/2010JTECHA1468.1.

Moisseev, D. N., and V. Chandrasekar, 2007: Examination of the μ–Λ relation suggested for drop size distribution parameter. *J. Atmos. Oceanic Technol.,* **24,** 847–855, doi:10.1175/JTECH2010.1.

Munchak, S. P., and A. Tokay, 2008: Retrieval of raindrop size distribution from simulated dual-frequency radar measurements. *J. Appl. Meteor. Climatol.,* **47,** 223–239, doi:10.1175/2007JAMC1524.1.

——, and C. D. Kummerow, 2011: A modular optimal estimation method for combined radar-radiometer precipitation profiling. *J. Appl. Meteor. Climatol.,* **50,** 433–448, doi:10.1175/2010JAMC2535.1.

Nešpor, V., W. F. Krajewski, and A. Kruger, 2000: Wind-induced error of raindrop size distribution measurement using a

two-dimensional video disdrometer. *J. Atmos. Oceanic Technol.,* **17,** 1483–1492, doi:10.1175/1520-0426(2000)017<1483:WIEORS>2.0.CO;2.

Pruppacher, H. R., and J. D. Klett, 1978: *Microphysics of Clouds and Precipitation.* D. Reidel, 714 pp.

Rose, C. R., and V. Chandrasekar, 2006: A GPM dual-frequency retrieval algorithm: DSD profile-optimization method. *J. Atmos. Oceanic Technol.,* **23,** 1372–1383, doi:10.1175/JTECH1921.1.

Schönhuber, M., G. Lammer, and W. L. Randeu, 2007: One decade of imaging precipitation measurement by 2D-video-disdrometer. *Adv. Geosci.,* **10,** 85–90, doi:10.5194/adgeo-10-85-2007.

Seto, S., and T. Iguchi, 2011: Applicability of the iterative backward retrieval method for the GPM dual-frequency precipitation radar. *IEEE Trans. Geosci. Remote Sens.,* **49,** 1827–1838, doi:10.1109/TGRS.2010.2102766.

——, ——, and T. Oki, 2013: The basic performance of a precipitation retrieval algorithm for the Global Precipitation Measurement Mission's single/dual-frequency radar measurements. *IEEE Trans. Geosci. Remote Sens.,* **51,** 5239–5251, doi:10.1109/TGRS.2012.2231686.

Smith, P. L., and D. Kliche, 2005: The bias in moment estimators for parameters of drop size distribution functions: Sampling from exponential distributions. *J. Appl. Meteor.,* **44,** 1195–1205, doi:10.1175/JAM2258.1.

——, Z. Liu, and J. Joss, 1993: A study of sampling-variability effects in raindrop size observations. *J. Appl. Meteor.,* **32,** 1259–1269, doi:10.1175/1520-0450(1993)032<1259:ASOSVE>2.0.CO;2.

——, D. Kliche, and R. W. Johnson, 2009: The bias and error in moment estimators for parameters of drop size distribution functions: Sampling from gamma distributions. *J. Appl. Meteor Climatol.,* **48,** 2118–2126, doi:10.1175/2009JAMC2114.1.

Testud, J., S. Oury, R. A. Black, P. Amayenc, and X. K. Dou, 2001: The concept of "normalized" distribution to describe raindrop spectra: A tool for cloud physics and cloud remote sensing. *J. Appl. Meteor.,* **40,** 1118–1140, doi:10.1175/1520-0450(2001)040<1118:TCONDT>2.0.CO;2.

Ulbrich, C. W., 1983: Natural variations in the analytical form of the raindrop size distribution. *J. Climate Appl. Meteor.,* **22,** 1764–1775, doi:10.1175/1520-0450(1983)022<1764:NVITAF>2.0.CO;2.

——, 1985: The effects of drop size distribution truncation on rainfall integral parameters and empirical relations. *J. Climate Appl. Meteor.,* **24,** 580–590, doi:10.1175/1520-0450(1985)024<0580:TEODSD>2.0.CO;2.

——, and D. Atlas, 1985: Extinction of visible and infrared radiation in rain: Comparison of theory and experiment. *J. Atmos. Oceanic Technol.,* **2,** 331–339, doi:10.1175/1520-0426(1985)002<0331:EOVAIR>2.0.CO;2.

——, and ——, 1998: Rain microphysics and radar properties: Analysis methods for drop size spectra. *J. Appl. Meteor.,* **37,** 912–923, doi:10.1175/1520-0450(1998)037<0912:RMARPA>2.0.CO;2.

Wong, R. K. W., and N. Chidambaram, 1985: Gamma size distribution and stochastic sampling errors. *J. Climate Appl. Meteor.,* **24,** 568–579, doi:10.1175/1520-0450(1985)024<0568:GSDASS>2.0.CO;2.

Zhang, G., J. Vivekanandan, and E. A. Brandes, 2001: A method for estimating rain rate and drop size distribution from polarimetric radar measurements. *IEEE Trans. Geosci. Remote Sens.,* **39,** 830–841, doi:10.1109/36.917906.

——, ——, ——, R. Meneghini, and T. Kozu, 2003: The shape–slope relation in observed gamma raindrop size distributions: Statistical error or useful information? *J. Atmos. Oceanic Technol.,* **20,** 1106–1119, doi:10.1175/1520-0426(2003)020<1106:TSRIOG>2.0.CO;2.